Prediction of Supersonic/Hypersonic Viscous Flows Over Re-entry Vehicles and Decoys

Bilal A. Bhutta* and Clark H. Lewis†
VRA, Inc., Blacksburg, Virginia 24063

In this paper we discuss the background and applications of a new unified series of codes for predicting large angle-of-attack viscous supersonic/hypersonic flows over spherically blunt re-entry vehicles and decoys. The solution scheme used involves a viscous shock-layer code for the blunt nose region, whereas a new parabolized Navier-Stokes (PNS) technique is used for the afterbody region. This new three-dimensional PNS scheme is unconditionally time-like and does not require the use of any sublayer approximation. A new predictor-corrector solution technique has been used along with a new fully-implicit and crossflow-coupled shock-fitting procedure to address the large angle-of-attack problem and to predict the bow shock location as a part of the marching solution. Several test cases are presented for various multiconic geometries under zero and nonzero angles of attack. The results of these test cases are used to demonstrate the accuracy, efficiency, and robustness of the unified viscous shock-layer (VSL) and PNS solution scheme.

Nomenclature

CA = axial-force coefficient
CM = pitching-moment coefficient
CN = normal-force coefficient
h = static enthalpy of the mixture
k = mixture thermal conductivity, also the grid-point index in the ξ_3 direction
L = body length
ℓ = grid point index in the ξ_2 direction
M = Mach number
m = molecular weight
n = iteration number
P,p = static pressure
Pr = mixture Prandtl number
Re = Reynolds number, $(\rho VRn)/\mu$
RN,Rn = nose radius
T = static temperature
u = x component of mass-averaged velocity
v = y component of mass-averaged velocity
w = z component of mass-averaged velocity
X,x = coordinate along body axis
x_j = x,y, and z for $j=1,2$, and 3
XCP = axial location of the center of pressure
α = angle of attack
ϵ = M_∞/Re_∞
ϕ = circumferential angle measured from the windward pitch plane
χ = intermediate solution vector
ξ_1 = marching or streamwise coordinate
ξ_2 = coordinate measured from the body to the outer bow shock
ξ_3 = coordinate measured from the windward pitch plane to the leeward direction
ρ = mixture density
μ = mixture viscosity

Superscripts

n = index for iteration
j = index in ξ_1 direction

Subscripts

, = represents partial derivative
∞ = freestream quantity
j,k,l = indicial notation representing 1, 2, and 3

Vector and Matrix Notation

Matrix = bold upper-case character
Vector = bold lower-case character
• = vector dot product

Introduction

OVER the past several years increased interest has been devoted to the field of computational fluid dynamics and aerothermodynamics. As computational capabilities become more and more powerful and accessible, numerical techniques for predicting flowfields around realistic re-entry configurations are becoming accurate and cost-effective means of obtaining the necessary aerothermodynamic data. This argument is even more valid today when the costs of ground-based experimental tests have become (and will continue to be) very high. At the same time, as the re-entry vehicles become more and more sophisticated, the available flight data (if any) can no longer suffice to represent the entire flight regime encountered by re-entry vehicles. It is indeed true that the numerical techniques cannot totally replace the need for experimental data. However, accurate numerical predictions can indeed augment the available data base by extrapolating to flight conditions where no experimental data may be available.

The existing methodology for predicting hypersonic external flows over three-dimensional geometries consists of Navier-Stokes (NS), parabolized Navier-Stokes (PNS), and viscous shock-layer (VSL) schemes. The NS schemes (Sahu,[1,2] Sahu and Nietubicz,[3] Richardson,[4] and Kumar[5]) are typically very time consuming and not well suited for various parametric studies required for design and analysis purposes. On the other hand, the existing noniterative PNS schemes (Weinacht et al.,[6] Kaul and Chaussee,[7] and Stalnaker[8]) suffer from instabilities and inaccuracies. Apart from being noniterative, such PNS schemes require a substantial approximation in the

Presented as Paper 89-0028 at the AIAA 27th Aerospace Sciences Meeting, Reno, NV, Jan. 9-12, 1989; received Jan. 26, 1989; revision received Dec. 26, 1989.

*Chief Scientist. Member AIAA.
†President. Associate Fellow AIAA.

way the subsonic sublayer region is treated. There are generally large global conservation-of-mass (as well as momentum and energy) errors associated with these PNS methods, which originate from the basic solution scheme. The existing VSL schemes (Murray and Lewis,[9] Thareja et al.,[10,11] Thompson et al.,[12] Kim et al.,[13,15] Swaminathan et al.,[14] and Song and Lewis[16]) have a basic limitation of being parabolic in the crossflow direction and, consequently, cannot march through crossflow separated regions. This prevents the VSL scheme from accurately predicting the aerodynamic response of complex ballistic configurations, which may experience strong crossflow separation either due to a large angle-of-attack condition or simply due to the three-dimensional nature of the geometry being considered (such as finned configurations, etc.). However, even under these conditions the flowfield in the nose region is attached, and the VSL schemes represent an accurate and efficient way of generating the nose solutions for starting other (more accurate) afterbody methods that can treat crossflow separation (such as the PNS schemes).

Most of the available computational schemes for predicting viscous hypersonic external flows are as different in their required input as they are in their basic formulation and final application. Furthermore, the file/disk manipulations required by these codes can also be quite different. The ease of using a particular code is not a major concern when one is working with one code and has used it frequently enough to develop a fair amount of familiarity with the code input and output. However, the production environment is a completely different situation. In a production environment the operational ease and user-friendliness of a code are almost always the deciding factors in establishing its value and subsequent usage, assuming of course that the code gives accurate predictions.

The term "production environment" implies that it is the final result that is of consequence and not the code(s); that is to say, the particular codes are looked at as only the tools to obtain the desired data. This means that, in general, most users are not expected to understand the fine points and intricacies of the code(s) involved. This motivation is even more appropriate when the user is to use several of such codes to obtain different parts of the data base finally needed. Thus, it is desirable to minimize the user interaction with the codes to be used. When in a production-type environment there are several codes to be used either independently or in a sequence, it becomes desirable to have what one could call a "master driver." The main objective is to provide a user with as much of a code-independant environment as possible. Furthermore, the master driver should have a modular structure, such that additional codes can be added to the selection when needed.

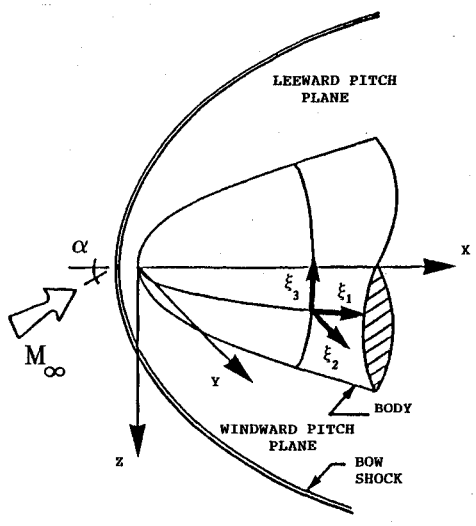

Fig. 1 Coordinate system.

In this paper we will present the use and applicability of a series of unified codes available in the VRAM (VRA Master) driver program, for predicting and analyzing viscous supersonic/hypersonic flows over spherically blunt multiconics or lifting configurations, from the nose tip to the body end. The accuracy, efficiency and ease-of-use of these codes will be discussed in detail, and comparisons will also be made with other available schemes in terms of solutions accuracy and computing efficiency.

Solution Scheme

The complete mathematical and numerical development of the PNS scheme used in the VRAM program has been discussed in detail by Bhutta and Lewis[17-22] and Bhutta et al.[23,24] The following sections provide a brief overview of the general approach used in formulating this PNS scheme.

The coordinate system used for the present three-dimensional PNS scheme is a general curvilinear coordinate system (ξ_1,ξ_2,ξ_3). Also, a body-fixed orthogonal (Cartesian) coordinate system is chosen such that the origin of the Cartesian coordinate system is at the tip of the blunt nose, and the x axis is aligned with the axis of the body. The ξ_1 coordinate is along the body and is also the marching direction. The ξ_2 coordinate stretches from the body to the outer bow shock and lies in an axis-normal plane. The ξ_3 coordinate is measured in the crossflow direction from the windward pitch plane (see Fig. 1).

The density (ρ), the density-velocity products (ρu, ρv, and ρw), the density-temperature product (ρT), and the pressure (p) are chosen as the flowfield unknowns. Thus, the final vector of unknowns becomes

$$q=[\rho,\ \rho u,\ \rho v,\ \rho w,\ \rho T,\ p]^T \tag{1}$$

Following the approach of Peyert and Viviand[25] and neglecting streamwise (ξ_1) dissipation effects, the nondimensionalized parabolized Navier-Stokes equations can be written in the following vectorial form:

$$f_{j,\xi_j}-\epsilon s_{2,\xi_2}-\xi s_{3,\xi_3}=h \tag{2}$$

These five equations representing the differential conservation of mass, momentum, and energy are mathematically closed by using the equation of state for the gas mixture. For perfect-gas as well as equilibrium-air and finite-rate chemically reacting gas models, this equation of state can be written in a nondimensional form as

$$\gamma p-Z^*\rho T=0 \tag{3}$$

where $Z^*=1$ for a perfect gas, $Z^*=Z^*(p,T)$ for equilibrium-air, and $Z^*=\dot{m}_\infty/\dot{m}$ for a finite-rate chemically reacting gas model.

If we assume that the solution at the "$n+1$" iteration is close to the solution at the nth iteration, we can use a first-order Taylor series expansion around the previous (nth) iteration to write Eq. (2) as

$$\begin{aligned}&(A_1/\Delta\xi_1-A_0)^n\cdot\Delta q^{n+1}+(A_2^n\cdot\Delta q^{n+1})_{,\xi_2}+(A_3^n\cdot\Delta q^{n+1})_{,\xi_3}\\&\quad-\epsilon(M_2^n\cdot\Delta q^{n+1})_{,\xi_2}-\epsilon(M_3^n\cdot\Delta q^{n+1})_{,\xi_3}\\&\quad=-[f_{j,\xi_j}-\epsilon s_{2,\xi_2}-\epsilon s_{3,\xi_3}-h]^{j+1,n}=g^{j+1,n}\end{aligned} \tag{4}$$

where

$$\Delta q^{n+1}=q^{j+1,n+1}-q^{j+1,n} \tag{5}$$

and two-point backward-differenced approximations have been used for the streamwise derivatives. It has been shown by Bhutta and Lewis[17-22] that, for the iterative process of Eq. (4), this simple two-point streamwise differencing is conservative

in the limit of convergence. This is not only important from a storage point of view, but it also gives the present scheme a significantly improved capability for treating strong compression discontinuities.

Equations (2) and (4) are elliptic in the ξ_2 and ξ_3 directions, so that central-differenced approximations are used for all ξ_2 and ξ_3 derivatives. However, the use of central-differenced schemes is typically associated with solution oscillations (Bhutta and Lewis,[17-22] Kaul and Chaussee,[26] Schiff and Steger,[27] and Shanks et al.[28]). Additional higher-order dissipation effects are needed to suppress such numerical solution oscillations. For this purpose, Bhutta and Lewis[17-22] and Bhutta et al.[23,24] have developed second- as well as fourth-order-accurate fully implicit smoothing approaches that are accurate and simple to use.

For the perfect-gas case, the air viscosity is obtained using the Sutherland formula (White[29]). The specific-heat ratio is assumed to be a constant (1.4 for air). The Prandtl number is also assumed fixed (0.72 for air), and the thermal conductivity is obtained from the definition of the Prandtl number. In the case of equilibrium chemically reacting air, the mixture thermodynamic and transport properties are provided in the form of a table. The thermodynamic properties involve the mixture enthalpy $h(p,T)$ and mixture density $\rho(p,T)$ data and are based on the tabular data of Miner et al.[30] The transport properties involve the mixture viscosity $\mu(p,T)$ and thermal conductivity $k(p,T)$ data based on the data developed by Peng and Pindroh.[31] The Prandtl number $Pr(p,T)$ data were obtained using these thermodynamic and transport property data. Additional details about these tabular data have been given by Bhutta and Lewis[21] and Bhutta et al.[24] In general, this equilibrium-air thermodynamic and transport property table covers the temperature range of 10–15000 K and the pressure range of 0.0025–15.849 atm. It should be noted that this range adequately covers most of the flight regime in which the equilibrium-air effects may be important. The nonequilibrium formulation of this three-dimensional PNS scheme has been discussed in detail by Bhutta and Lewis[22]and Bhutta et al.[23]

Using two-point streamwise differencing and central-differenced approximations in the ξ_2 and ξ_3 directions, the final differenced equations corresponding to the fluid mechanics problem are written in the block-pentadiagonal form, as given in Eqs. (4). It should be noted that the right-hand-side terms of Eqs. (4) are the governing differential equation corresponding to the fluid mechanics problem written at the nth iteration level, and they go to zero in the limit of convergence. As discussed by Bhutta and Lewis[17-22] and Bhutta et al.,[23,24] under these conditions the exact form of these implicit left-hand-side terms only affects the convergence path and not the converged solution. With this idea in mind, the implicit left-hand matrices of Eqs. (4) are not updated after the first few iterations. Furthermore, the new predictor-corrector solution scheme of Bhutta and Lewis[21,22] has also been used to treat the strong crossflow coupling effects that may exist, due either to the three-dimensional nature of the geometry or to large angle-of-attack conditions.

The problem represented by the governing PNS equations is a split-boundary-value problem; i.e., the equations are hyperbolic-parabolic in the ξ_1 direction and elliptic in the ξ_2 and ξ_3 directions. The initial conditions to start the PNS solutions are obtained from appropriate VSL blunt-body solution schemes.[9-16] The VSL blunt-body solution is interpolated to obtain the starting solution at the initial data plane (IDP) for the three-dimensional PNS afterbody solution. The boundary conditions at the wall consist of six independent relations representing the nature of the gas mixture and the physical conditions at the wall. These conditions consist of no-slip boundary conditions, specified wall-temperature distribution, equation of state, and zero pressure derivative in the ξ_2 direction $(p,\xi_2=0)$. For a finite-rate chemically reacting gas model, the wall boundary conditions can be either ablating or nonablating wall boundary conditions. For a nonablating surface, the species wall boundary conditions can be fully catalytic or noncatalytic type.[22] For an ablating surface, the species wall boundary conditions assume an equilibrium-catalytic wall.[23]

The boundary conditions at the outer bow shock involve a fully implicit and crossflow coupled shock-fitting approach, and the bow shock is predicted as the solution marches down the body. The corresponding shock boundary conditions for nonequilibrium flows assume a frozen shock crossing. Currently, the three-dimensional PNS scheme being presented can only treat flows with a pitch plane of symmetry; i.e, the vehicle geometry is symmetric with respect to the pitch plane and there is no yaw. The symmetric and reflective boundary conditions used in this case are based on the second-order crossflow boundary conditions used by Kaul and Chaussee[26] and Shanks et al.[28]

Predictor-Corrector Solution Scheme

Under large angle-of-attack conditions strong crossflow separated regions may develop on the leeward side. Under these conditions, solution coupling in the crossflow direction is very important. If these coupling effects are not properly considered during the iterative solution, they can cause severe convergence difficulties. In order to address the problem of crossflow coupling, Bhutta and Lewis[21,22] have developed a new predictor-corrector solution scheme that is divided into three different parts: 1) the predictor step, 2) the fully implicit shock solution, and 3) the corrector step. The overall iterative process consisting of these three steps is repeated until the solution converges at all grid points, and then the solution moves on to the next marching step.

1) Predictor step: In the predictor step the implicit crossflow coupling effects are neglected in favor of the body-normal coupling effects. The equations are inverted from the body of the shock to develop a recursive relationship between the solution at successive grid points in the axis-normal direction.

2) Fully-implicit crossflow-coupled shock solution: In developing this bow shock-fitting scheme, it is assumed that from one iteration to the next the shock points move along the ξ_2 grid line. This assumption reduces the number of unknowns to be solved, and the final solution has only one additional unknown at the shock, which completely defines the spatial movement of the shock point. This shock-fitting scheme has been discussed in detail by Bhutta and Lewis[20-22]; however, briefly speaking, using Δ_s to denote the amount by which the shock point moves in the ξ_2 direction, the corresponding movement of the shock-point coordinates from one iteration to the next can be written as

$$(x_j)_s^{n+1} \simeq (x_j)_s^n + (x_{j,\xi_2})_s^n (\Delta)_s^{n+1} \tag{6}$$

Thus, there are actually seven unknowns at the shock, written in a vectorial form as

$$q_s = [\rho, \rho u, \rho v, \rho w, \rho T, p, \Delta]_s^T \tag{7}$$

The Rankine-Hugoniot shock-crossing equations (representing the conservation of mass, momentum, and energy) provide five of the seven equations needed to close the system of equations at the shock. One of these additional equations is the equation of state of the gas, and the other equation is provided by applying the differential continuity-of-mass equation behind the shock. As we see, in this approach, no approximation other than the assumption of a frozen or equilibrium-air Rankine-Hugoniot shock has been used. These equations are equally valid whether the conditions behind the shock are viscous or inviscid dominated or whether substantial flowfield gradients exist behind the shock.

Using the recursive relation from the predictor step at ℓ=(LMAX-1) location, the seven shock-fitting equations are solved to obtain the solution at the shock. Using this shock-

point solution and the recursive relations of the predictor step, the predictor solution can now be obtained for all interior grid points. This predictor solution is then used to solve the final corrector step. Furthermore, once the solution at the shock has been obtained, the x, y, and z coordinates of the new shock point locations are determined from Eqs. (6), and the grid is updated for the next iteration.

3) Corrector step: Just like the shock-point solution, the solution in the corrector step uses the recursive relations from the predictor step to eliminate the $(k,\ell-1)$ contributions in the difference molecule. Then, assuming that the solution at the $(k,\ell+1)$ point can be reasonably approximated from the predictor step, one can reduce the governing pentadiagonal system of equations to only a coupled system in the crossflow direction. This implicit crossflow solution is obtained using plane-of-symmetry boundary conditions applied in the windward and leeward pitch planes. In this way, the flowfield solution is marched from the shock to the body.

Capabilities and Limitations of the VRAM Programs

This section gives a brief overview of the various capabilities as well as limitations of the various VSL/PNS codes involved in the VRAM driver program. These capabilities and limitations are given below.

1) Gas models: perfect-gas model, equilibrium-air gas model, nonequilibrium-air gas model, nonequilibrium Teflon/carbon-air gas model.

2) Flight altitude: 0 < flight altitude ≤ 300 kft.

3) Flight Mach number: 2 ≤ flight Mach number ≤ 35.

4) Angle of attack: 0 ≤ angle of attack ≤ 25 deg.

5) Vehicle geometry: spherically blunted three-dimensional geometries without axial separation.

6) Nose radius: nose radius ≥ 0.01 in.

7) Reynolds number: freestream Reynolds number based on nose radius > 100.

8) Flow type: fully laminar, transitional, or fully turbulent flows.

9) Wall boundary conditions, ablating or nonablating surfaces, adiabatic wall, isothermal wall, specified wall-temperature distribution, fully, finite, or noncatalytic wall for nonequilibrium air, or equilibrium-catalytic wall for ablating nonequilibrium flow.

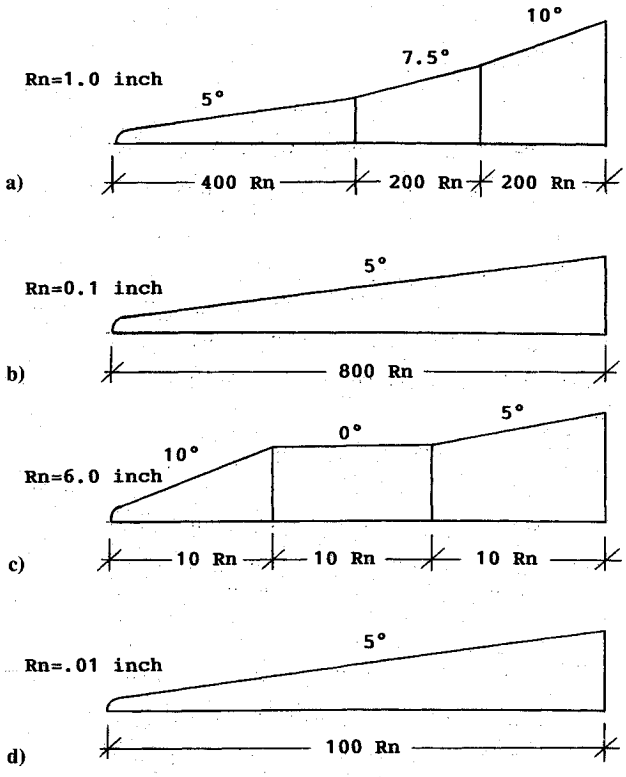

Fig. 2 Vehicle geometries for cases 1-6.

Table 1 Classification of cases 1-6

Test case	Mach number	Alt., kft	Gas model[a]	Flow type	AOA,[a] deg	TWALL, R	Vehicle geometry
1a[b]	20.0	164.05	PG	LAM	0.0	2000.0	Fig. 2a
1b	20.0	164.05	EQ	LAM	0.0	2000.0	Fig. 2a
2a[c]	20.0	100.00	PG	TRN	0.0	2000.0	Fig. 2a
2b[c]	20.0	100.00	EQ	TRN	0.0	2000.0	Fig. 2a
3a	20.0	100.00	PG	LAM	5.0	2000.0	Fig. 2b
3b	20.0	100.00	EQ	LAM	5.0	2000.0	Fig. 2b
4	25.0	275.00	PG	LAM	0.0	2000.0	Fig. 2c
5[d]	20.0	200.00	PG	LAM	0.0	2000.0	Fig. 2d
6[e]	20.0	125.00	NEQ	LAM	0.0	2000.0	Fig. 2d

[a] PG = perfect gas model; EQ = equilibrium-air gas model; NEQ = nonequilibrium Teflon-air gas model; LAM = laminar flow; TRN = transitional flow; AOA = angle of attack; TWALL = wall temperature.
[b] Turbulent-viscosity calculations were based on the two-layer eddy-viscosity model of Cebeci and Smith, with the edge conditions determined using a total enthalpy model.
[c] For cases 2a and 2b the transition to turbulence occurred instantaneously at $X/RN = 10$.
[d] Nose radius for cases 5 and 6 was 0.01 in.
[e] Case 6a was nonablating with 2000 R wall temperature, whereas cases 6b–6e had surface ablation for $x > 5Rn$. Wall temperature for ablating region was kept fixed at 1800 R.

Sample Results and Discussion

Some sample results for flowfield predictions over multiconic RV and decoy configurations under moderate angle-of-attack conditions are discussed in this section, and additional results for large angle-of-attack conditions have been discussed by Bhutta and Lewis.[20-22] The multiconic test cases considered (cases 1-6) are defined in Table 1, and the vehicle configurations are shown in Fig. 2. The starting solutions for these calculations were provided using a perfect gas/equilibrium-air VSL solution scheme. These calculations include laminar as well as turbulent flow conditions, and both perfect-gas and equilibrium-air gas models were used. The test cases of laminar perfect-gas flows at 0- and 5-deg angles of attack have been compared with results obtained from the Air Force Wright Aeronautical Laboratories (AFWAL) PNS code (Neumann and Patterson[32]).

A comparison of the wall pressure distributions for the laminar perfect-gas and equilibrium-air calculations of cases 1a and 1b is shown in Fig. 3; the corresponding heat transfer predictions are shown in Fig. 4. Since the equilibrium-air results from the AFWAL PNS code may not be reliable, we did not attempt to compare the VRA PNS equilibrium-air results with the AFWAL code results. As can be seen from these figures, the various wall-measurable quantities are very well behaved. The effect of the gas model on the wall pressure distributions is less than 5% in the over-expansion and recompression region, and it is less than 1% over most of the body length. The effect of the VRA PNS equilibrium-air gas model on the wall heat transfer distribution is to increase the heat transfer rate by 20–25% over the corresponding perfect-gas predictions. The difference in perfect-gas wall pressure distribution for the VRA PNS and AFWAL PNS codes is almost negligible. The corresponding difference in the heat transfer rate distribution is very small, except near the over-expansion and recompression region. In general, the agreement is excellent. Figure 5 shows the wall heat transfer rate predictions under turbulent flow conditions, with transition to turbulence occurring instantaneously at $x = 10Rn$. Again, it can be seen that with the VRA PNS equilibrium-air gas model, the wall heat transfer predictions increase by 20–25% over the corresponding perfect-gas predictions.

The wall pressure and wall heat transfer predictions for the 5-deg angle-of-attack laminar case 3 calculations with perfect-gas and equilibrium-air gas models are shown in Figs. 6 and 7.

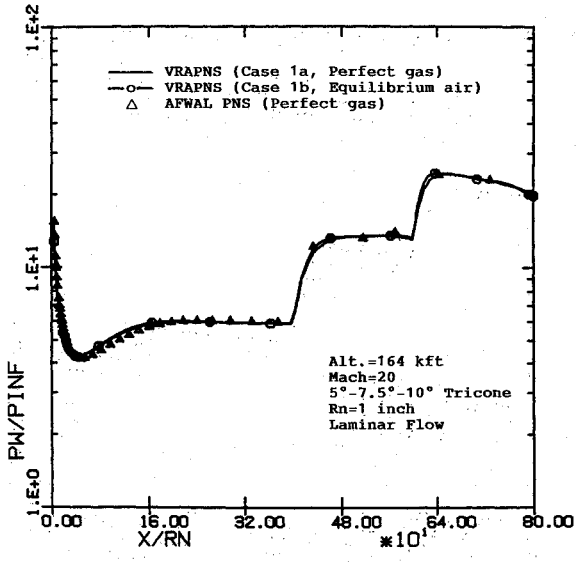

Fig. 3 Wall pressure distribution for case 1a and 1b.

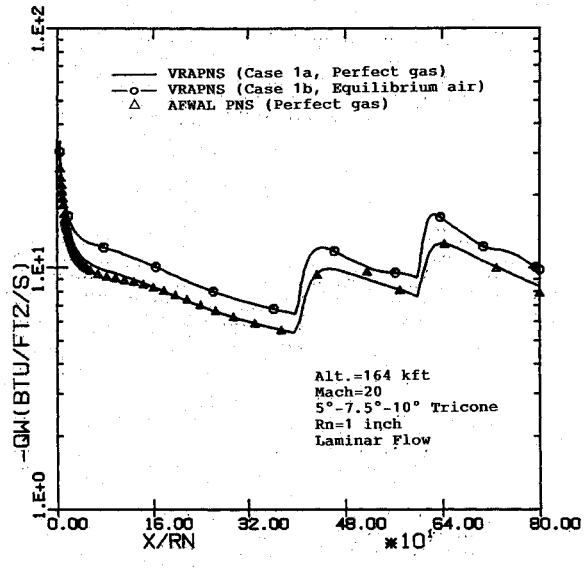

Fig. 4 Heat-transfer rate distribution for case 1a and 1b.

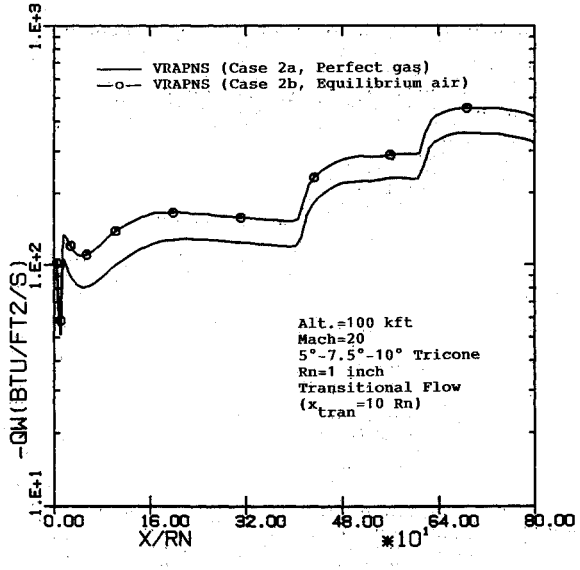

Fig. 5 Heat-transfer rate distribution for case 2a and 2b.

These results show that the effects of the gas model on the wall pressure distribution are very small. The only noticeable differences in the wall pressure are on the leeside, where the effect of the equilibrium-air gas model is to decrease the wall pressure distribution by nearly 10%. The wall heat transfer predictions using the VRA PNS equilibrium-air gas model are 20–25% greater than the corresponding perfect-gas predictions.

Extreme care should be taken to obtain a meaningful flowfield solution from the AFWAL PNS code, since it is very difficult to choose optimum parameters unless one conducts parametric studies by varying various parameters (Neumann and Patterson[32]). In our computation with the AFWAL PNS code, we chose the important parameters, according to Patterson's suggestions.[33]

To obtain a more accurate flowfield solution with the AFWAL PNS code, we had to use a large number of crossflow planes (minimum of 19, and typically 45) for simple axisymmetric geometries at nonzero angles of attack. We attempted to compute case 3a (5-deg angle of attack) with 45 crossflow planes; however, we experienced some solution difficulties around $360Rn$ to $420Rn$ down the body length. Therefore, only the result from the AFWAL 19-plane solution was com-

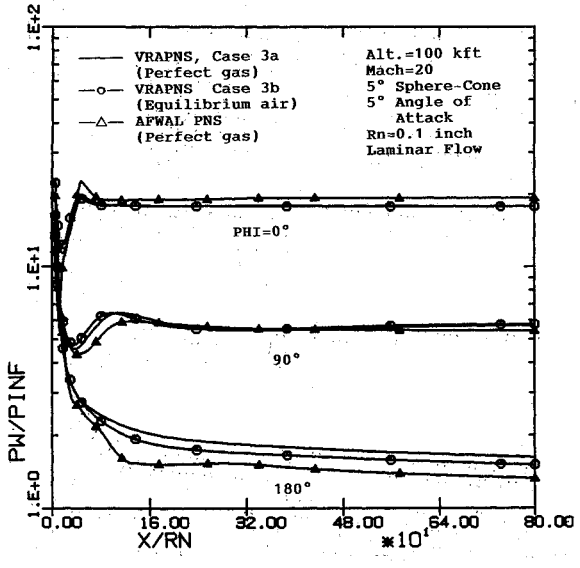

Fig. 6 Wall pressure distribution for case 3a and 3b.

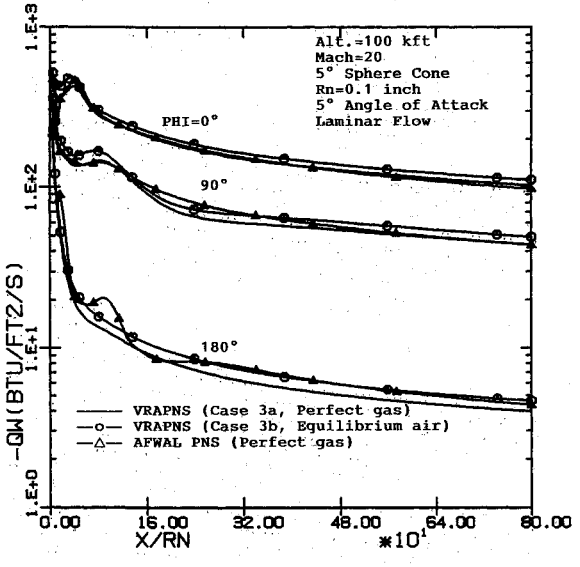

Fig. 7 Heat-transfer rate distribution for case 3a and 3b.

pared with that from the VRA PNS 9-plane solution. The windward wall pressure differences between the 19-plane AFWAL PNS and 9-plane VRA PNS solutions was less than 8%; however, with the 45-plane AFWAL PNS solution, the difference was much smaller than 8%. There was almost negligible difference in side-plane ($\phi = 90$ deg) solution. The leeside ($\phi = 180$ deg) shows a much larger difference in wall pressure prediction, but with the 45-plane AFWAL PNS solution the difference was much less than that with 19 planes.

The heat transfer rate comparison shows small differences in the windward and side planes; however, the leeward plane shows larger difference around $x = 100Rn$. But, as we approach the body end, these differences become less than a few percentage points. The corresponding wall heat transfer predictions for the high-altitude laminar case 4 calculations, using a perfect-gas model, are shown in Fig. 8.

To demonstrate the capabilities of the VRAM series of codes to predict flowfields over decoy-like vehicles, we computed the flow over a zero lift, 5-deg half-angle spherically blunted cone with a nose radius of 0.01 in. at Mach 20 and altitude of 200 kft. Under these conditions, the freestream Reynolds number based on nose radius was 27.6 or much less than the recommended lower limit of 100 indicated earlier in this paper. This case was included to show that decoy-like noses at low Reynolds numbers (high altitude) can also be treated with our VSL and PNS schemes.

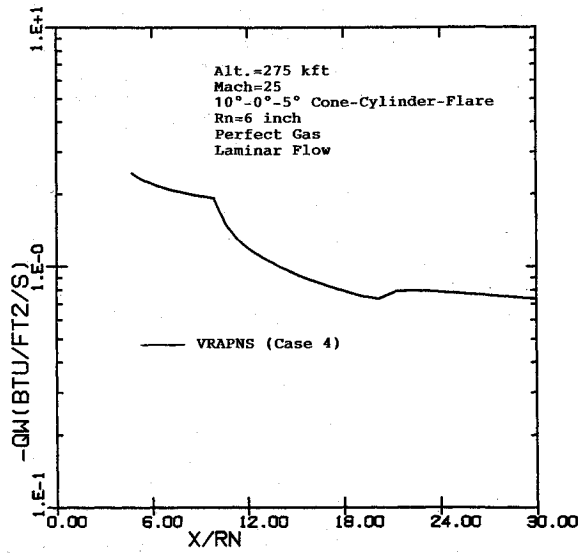

Fig. 8 Heat-transfer rate distribution for case 4.

Table 2 Force and moment data for cases 1-6

Case	*CA*	*CN*	*−CM*	*XCP/L*
1a	0.07226	—	—	—
1b	0.07451	—	—	—
2a	0.08508	—	—	—
2b	0.09027	—	—	—
3a	0.03658	0.16149	0.11013	0.68200
3b	0.03735	0.16220	0.11061	0.68189
4	0.36681	—	—	—
5	1.12800	—	—	—
6a	0.17350	—	—	—
6b	0.09307	—	—	—
6c	0.09301	—	—	—
6d	0.09394	—	—	—
6e	0.09472	—	—	—

The pressure distribution predicted for these case 5 conditions is shown in Fig. 9. Because of the low Reynolds number flow over the cone, it was desirable to iterate globally the VSL nose solution three times to improve the VSL and resulting IDP solution to start the PNS downstream solution. Also, since the normal momentum equation in the VSL technique does not contain any viscous terms, there is a mismatch in the VSL and PNS predictions that becomes large as the Reynolds number becomes very small—as in this case. For conditions such as these, we move the IDP further downstream from the nose (around $x = 45Rn$) than where we would typically locate it for high Reynolds number flows (around $x = 4.5Rn$). By moving the IDP downstream, we reduce the effects of the mismatch in VSL and PNS normal momentum equations, but we cannot completely eliminate its effects on the IDP. In Fig. 9, the bump in the pressure distribution downstream of the IDP at $45Rn$, as shown, is caused by this mismatch. However, as shown in Fig. 10, it is interesting to note that the effect of the mismatch in normal momentum equations is smaller on the heat-transfer distribution than on the pressure distribution. In this case, the surface heat transfer distribution is much smoother and less affected by the mismatch.

The force and moment data at the body end for these test cases are shown in Table 2. The prediction of the axial force coefficient for case 5 is apparently too high. Of course, because of the very low Reynolds number ($Re_\infty = 27.6$) in this case, the effects of wall and shock slip should have been considered. When included, these wall and shock slip effects tend to decrease the vehicle drag. Again, without appropriate wall

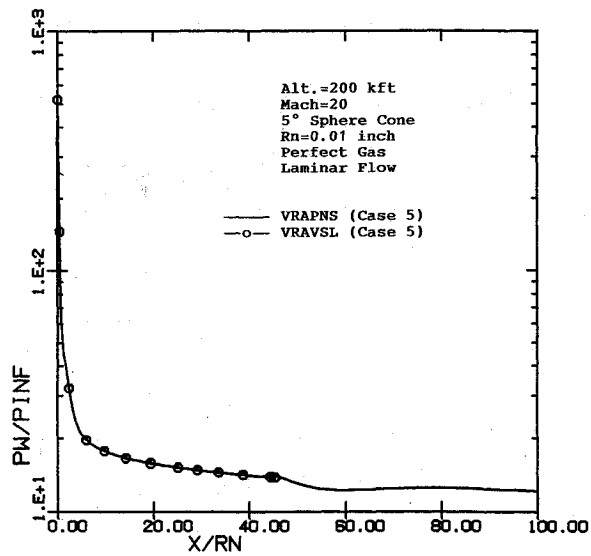

Fig. 9 Wall pressure distribution for case 5.

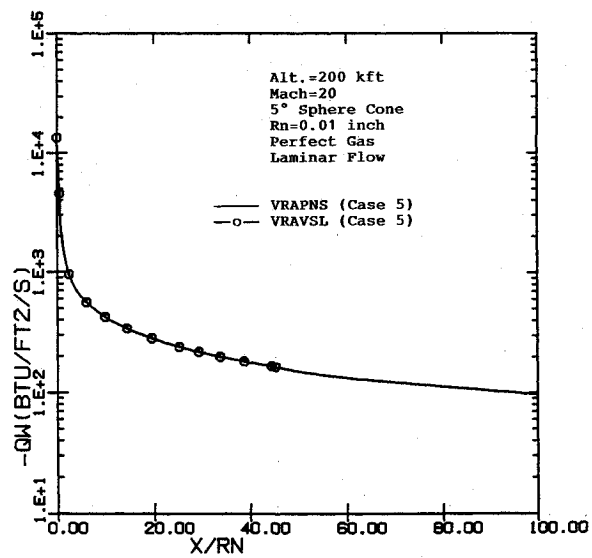

Fig. 10 Heat-transfer rate distribution for case 5.

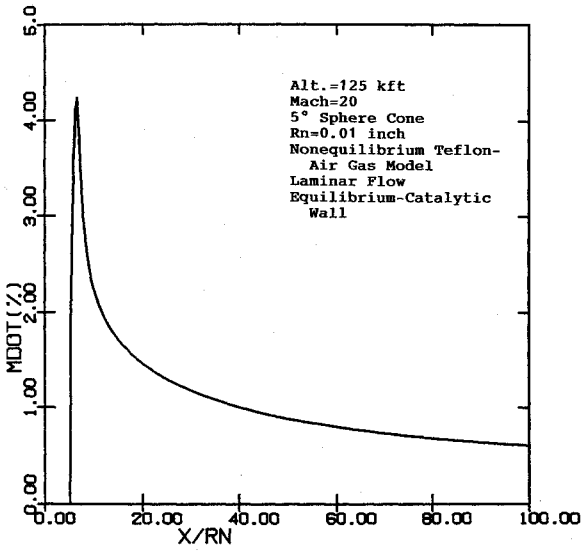

Fig. 11 Surface ablation rate distribution for case 6.

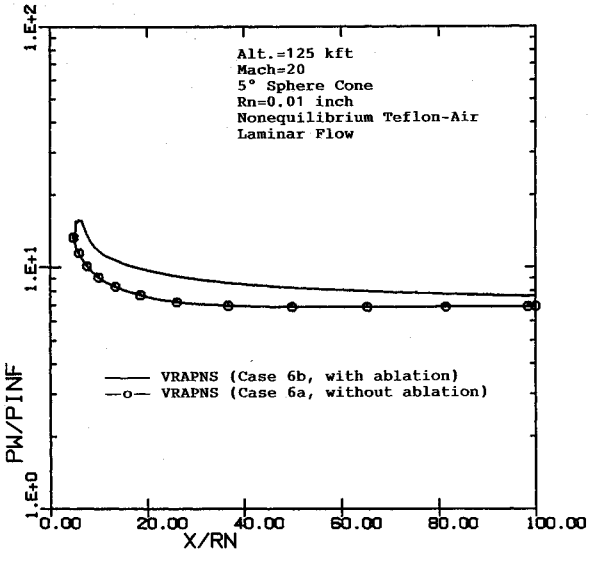

Fig. 12 Wall pressure distribution for case 6.

and shock slip models, we do not recommend the use of the present PNS scheme for such low Reynolds numbers; however, with this low Reynolds number case 5 calculation, we do hope to demonstrate a numerical capability that we believe may be unique.

The results of calculations for case 6 are shown in Figs. 11-16. The geometry for these case 6 calculations is the same as the one used for case 5 (see Fig. 2) and consists of a 5-deg sphere-cone vehicle with a 0.01-in. nose radius. The freestream conditions consist of zero angle-of-attack, Mach 20 flow at a flight altitude of 125 kft. The gas model consists of a finite-rate chemically-reacting Teflon-air gas mixture with and without Teflon ablation at the surface. In case of surface ablation, the nose is nonablating and ablation starts at $x=5Rn$. This nonequilibrium Teflon-air gas model and the associate equilibrium-wall-ablation boundary conditions have been discussed in detail by Bhutta et al.[34]

The case 6a calculations involved no wall ablation; cases 6b-6e involved Teflon surface ablation and used different computational grids. The various grid sizes used are shown in Fig. 3; however, briefly speaking, cases 6a and 6b used 50 points between the body and shock and a maximum marching step size of $5Rn$. Case 6c used 150 points between the body and the shock and a maximum marching step size of $5Rn$. Cases 6d and 6e used 50 points between the body and the shock and maximum marching step sizes of $1Rn$ and $0.1Rn$, respectively.

The axial distribution of the surface ablation rate used for these case 6 calculations is shown in Fig. 11. The effects of surface ablation on the wall pressure are shown in Fig. 12, whereas the corresponding effects on the surface heat-transfer rate are shown in Fig. 13. Figure 12 shows that, under these conditions, there is significant effect of surface ablation on the wall pressure distribution. In general, surface ablation increases the wall pressure and, by the body end, the wall pressure with ablation is approximately 11% higher than the corresponding case without ablation. This difference is even larger in the forebody region. Figure 13 shows that the wall heat transfer rate with surface ablation is much lower than without ablation. For the case with ablation, there is a sudden increase in the wall heat transfer at the point where surface ablation starts. This is due to the abrupt change in the near-wall species concentrations due to Teflon ablation and, thus, the increased surface heat transfer due to species diffusion. The corresponding component of wall heat transfer due to conduction is much smaller than in the case of a nonablating

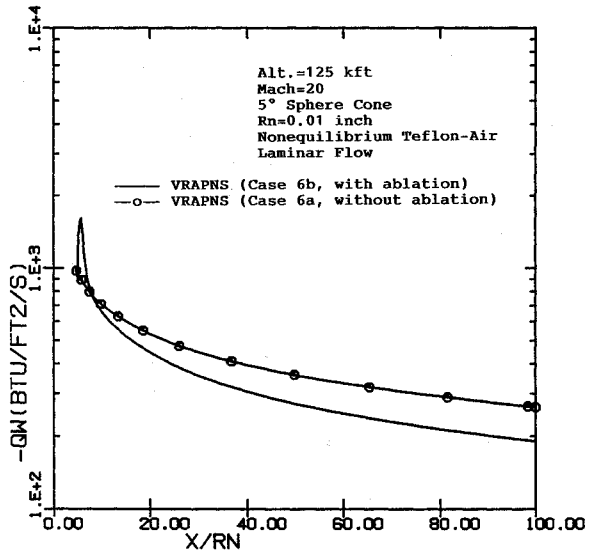

Fig. 13 Heat-transfer rate distribution for case 6.

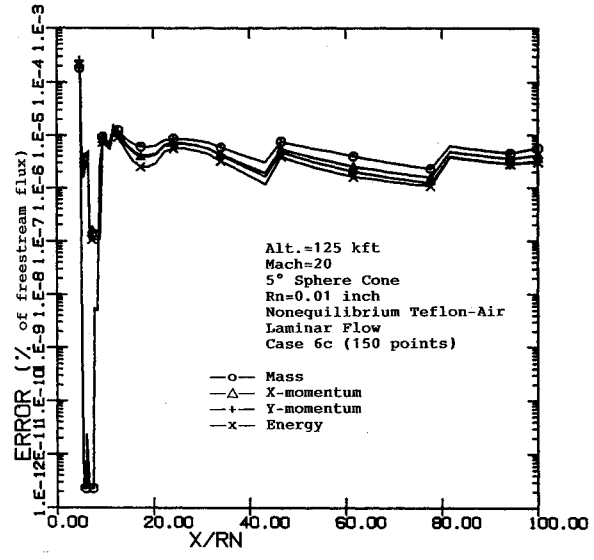

Fig. 14 Global conservation errors for case 6c.

Table 3 Computing-time estimates for cases 1-6

Case	PNS grid size ($N1 \times N2 \times N3$)[a]	Time, min:s[b] Time[c] Nose	PNS	Total	CPU
1a	121×150× 1	0:15	1:20	1:35	0:40
AFWAL	2673× 90× 3	0:15	28:36	28:51	14:18
1b	161×150× 1	0:45	2:02	2:47	1:01
2a	124×150× 1	0:16	1:29	1:45	0:45
2b	130×150× 1	0:44	1:40	2:24	0:50
3a	101× 50× 9	0:43	4:39	5:22	2:20
AFWAL	1409× 90×19	0:43	57:46	58:29	30:24
3b	104× 50× 9	2:14	4:19	6:33	2:20
4	33×150× 1	0:24	0:36	1:00	0:18
5	71× 50× 1	0:24	0:15	0:39	0:08
6a	46× 50× 1	1:34	0:54	2:28	0:29
6b	46× 50× 1	1:34	1:25	2:55	0:45
6c	46×150× 1	1:34	4:48	6:22	2:34
6d	109× 50× 1	1:34	2:30	4:04	1:20
6e	955× 50× 1	1:34	15:51	17:25	8:27

[a] $N1$ = grid points in the streamwise direction; $N2$ = grid points between the body and the shock; $N3$ = grid points in the crossflow direction.
[b] These computing times are for IBM 3090 (Model 300E) with FORTVS2 compiler, using scalar OPT(3) optimization.
[c] PNS computing time estimate based on Cray 2, using CFT77 compiler.

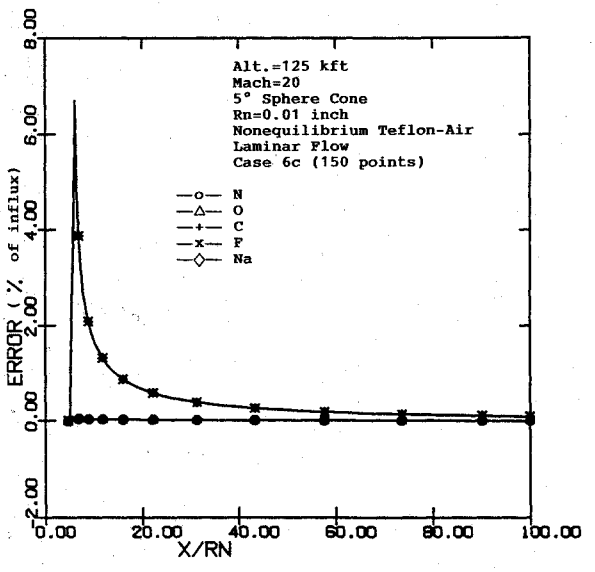

Fig. 15 Elemental mass conservation errors for case 6c.

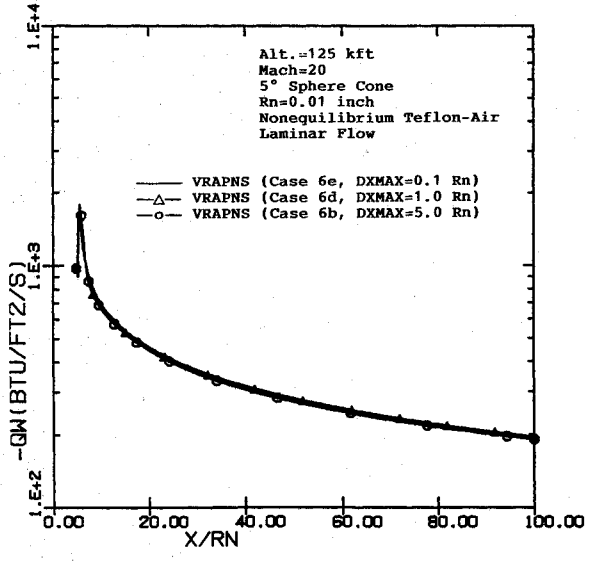

Fig. 16 Effects of axial step size on wall heat-transfer rate for case 6.

surface. As we move along the body, both diffusion- and conduction-related components of the wall heat transfer for the ablating case decrease quite rapidly. At the end of the body, the total wall heat transfer rate for the ablating case is 30% lower than the nonablating case. However, although not shown here, with Teflon surface ablation, the conduction component of wall heat transfer and also of skin friction for these conditions decrease by approximately a factor of 3. As far as the vehicle drag is concerned, surface ablation increases the pressure-induced drag by 11%; however, the friction component of the drag decreases by a factor of 2.5. Thus, as shown in Table 2, the total vehicle drag with Teflon surface ablation (case 6b) is approximately 1.9 times less than the total vehicle drag without ablation (case 6a).

An important aspect of the present Teflon-air PNS calculations is the accuracy with which the global conservation equations are satisfied. The errors in the global conservation of mass, x momentum, y momentum, and total energy for this case are shown in Fig. 14. The results shown are for the case 6c calculations, which use 150 points between the body and the shock, and used a convergence constraint of 0.001% on the flowfield variables and 0.01% for the chemical species. As can be seen from this figure, the global conservation of these flowfield quantities is satisfied to the order of the flowfield convergence constraint. In fact, the global conservation of these flowfield quantities can be further improved by tightening the flowfield convergence constraint. This is because the the global conservation of these flowfield quantities is directly implied by the differential conservation equations. The corresponding conservation of elemental species is shown in Fig. 15. Satisfying the elemental conservation accurately is quite difficult because the conservation of elemental species is only indirectly implied by the conservation of chemical species. In other words, in order to achieve good accuracy on global conservation of element mass, the differential species conservation equations and the differential flowfield (mass, momentum, and energy) conservation equations need to be satisfied even more accurately. As can be seen from Fig. 15, the conservation errors for the primary elemental species (N and O) are less than 0.03% of their mass, whereas for the trace species (C, F and Na) these errors are approximately 0.1% at the body end. The conservation errors shown in Fig. 15 for the trace species at any axial location are as a percentage of the local injected mass. Thus, at the start of surface ablation, these relative errors are large because the amount of their injected mass is very small.

The effects of axial step size on the surface heat-transfer rate for these case 6 conditions are shown in Fig. 16. This figure shows the results with maximum axial step sizes of $5.0Rn$ (case 6b), $1.0Rn$ (case 6d), and $0.1Rn$ (case 6e). The total marching steps involved for these cases were 46, 109 and 955, respectively. As can be seen from this figure, between cases 6b and 6e, the axial step size varies by a factor of 20; however, there is no identifiable effect on the predicted wall heat transfer. Table 2 shows that, for these calculations, the total axial force at the body end differs by no more than 1.7%. These results clearly show the stability and accuracy of the PNS marching scheme used in the VRAM driver.

Table 3 shows the computational grids used for these calculations and the corresponding computing times. The computing time for the AFWAL PNS code is also presented, along with VRA PNS results. Generally, to get results similar to our VRA PNS scheme, the AFWAL PNS code required approximately 15 to 25 times more computing time. We observed also that it was very difficult to start and run the AFWAL PNS solution completely when compared to our simple unified approach.

Concluding Remarks

A unified series of codes has been developed to study three-dimensional viscous hypersonic flows around spherically blunt multiconics under zero and nonzero angle-of-attack condi-

tions. The VRA PNS scheme was used to study perfect-gas and equilibrium-air flows around some typical multiconic RV and decoy configurations to demonstrate its accuracy, efficiency, and versatility. The results of these studies support the following comments.

Based on the axisymmetric perfect-gas PNS scheme of Bhutta and Lewis,[17] a new three-dimensional PNS scheme has been developed. This three-dimensional PNS scheme is unconditionally time-like in the subsonic as well as the supersonic flow regions and does not require the use of any sublayer approximation. Furthermore, the scheme permits very fine grids to be used in the near-wall region for improving solution accuracy.

This PNS scheme is capable of treating perfect-gas, equilibrium-air, and nonequilibrium finite-rate chemically reacting gas models with and without surface ablation. A new predictor-corrector solution scheme has been incorporated to treat the strong crossflow coupling effects in and around the crossflow separated regions (Bhutta and Lewis[21,22]), and a new fully implicit shock-prediction scheme has been used to accurately predict the bow shock location as the solution marches down the body (Bhutta and Lewis[21,23]). This scheme uses a general curvilinear coordinate system and predicts the correct shock location without having to make any approximation about the viscous or inviscid nature of the flow behind the shock. Furthermore, this shock-fitting solution is fully coupled in the crossflow direction and results in smoother and more accurate shock shapes, and the method has very good stability and convergence characteristics.

This PNS scheme uses a fourth-order accurate smoothing approach which is an extension of the earlier axisymmetric approach of Bhutta and Lewis.[17,18] In this approach, the crossflow smoothing effects are applied to all variables; however, the smoothing effects in the axis-normal direction are limited only to the pressure field. This results in accurate wall heat transfer and skin-friction predictions even with coarse grids in the axis-normal direction.

The results of studies conducted show that with a pseudo-unsteady algorithm, the present fully iterative three dimensional results can be obtained accurately and efficiently without any significant computing-time penalty. Furthermore, the enhanced solution accuracy permits much larger marching steps to be used, and this substantially reduces the final computing times.

Comparisons of predicted flowfields over multiconic configurations show that the results from the current approach provide a more stable prediction of surface-measurable quantities than the AFWAL PNS scheme with only a small fraction of the computing time (approximately 5%), and the VRA PNS required no variation of input parameters for a successful solution.

The current calculation of a decoy-like vehicle under extremely low Reynolds number (27.6) conditions demonstrated the successful application of the VRAM driver program and the associated PNS and VSL schemes for high-altitude and low-Reynolds-number flight conditions.

References

[1]Sahu, J., "Drag Predictions for Projectiles at Transonic and Supersonic Speeds," U.S. Army Ballistic Research Lab., Aberdeen Proving Ground, MD, BRL-MR-3523, June 1986.

[2]Sahu, J., "Three-Dimensional Base Flow Calculations for Projectile at Transonic Velocity," U.S. Army Ballistic Research Lab., Aberdeen Proving Ground, MD, BRL-MR-3610, June 1987.

[3]Sahu, J., and Nietubicz, C. J., "Improved Numerical Predictions of Transonic Flow," U.S. Army Ballistic Research Lab., Aberdeen Proving Ground, MD, BRL-TR-2784, March 1987.

[4]Richardson, P., "High-Speed Configuration Aerodynamic CFD," First National Aerospace Plane Technology Symposium, NASA Langley Research Center, Hampton, VA, May 1986.

[5]Kumar, A., "High-Speed Inlet Analysis," First National Aerospace Plane Technology Symposium, NASA Langley Research Center, Hampton, VA, May 1986.

[6]Weinacht, P., Guidos, B. J., Sturek, W. B., and Hodes, B. A., "PNS Computations of Spinning Shell at Moderate Angles of Attack and for Long L/D Finned Projectiles," U.S. Army Ballistic Research Lab., Aberdeen Proving Ground, MD, BRL-MR-3522, June 1986.

[7]Kaul, U. K., and Chaussee, D. S., "AFWAL Parabolized Navier-Stokes Code: 1983 AFWAL/NASA Merged Baseline Version," Flight Dynamics Lab., Air Force Wright Aeronautical Lab., Wright-Patterson AFB, OH, AFWAL-TR-83-3118, Oct. 1983.

[8]Stalnaker, J. F., "Improvements to the AFWAL PNS Code Formulation," Parabolized Navier-Stokes Workshop: Transitioning Numerical Fluid Mechanics to the Design Environment, Bergamo Center, Dayton, OH, Sept 1985.

[9]Murray, A. L., and Lewis, C. H., "Hypersonic Three-Dimensional Viscous Shock-Layer Flows Over Sphere-Cones at High Altitudes and High Angles of Attack," Virginia Polytechnic Institute and State University, Blacksburg, VA, VPI&SU AERO-078, Jan. 1978.

[10]Thareja, R. R., Szema, K. Y., and Lewis, C. H., "Chemical Equilibrium Laminar or Turbulent Three-Dimensional Viscous Shock-Layer Flows," *Journal of Spacecraft and Rockets,* Vol. 20, No. 5, Sept. 1983, pp. 454–460.

[11]Thareja, R. R., Szema, K. Y., and Lewis, C. H., "Viscous Shock-Layer Predictions for Hypersonic Laminar or Turbulent Flows in Chemical Equilibrium over the Windward Surface of a Shuttle-Like Vehicle," *Progress in Astronautics and Aeronautics: Entry Vehicle Heating and Thermal/Protection Systems: Space Shuttle, Solar Starstrobe, Jupiter Galileo Probe,* Vol. 85, edited by P. E. Bauer and H. E. Collicott, AIAA, New York, 1983.

[12]Thompson, R. A., Lewis, C. H., and Kautz, F. A., II, "Comparison Techniques for Predicting 3-D Viscous Flows Over Ablated Shapes," AIAA Paper 83-0345, Jan. 1983.

[13]Kim, M. D., Bhutta, B. A., and Lewis, C. H., "Three-Dimensional Effects Upon Real Gas Flows Past the Space Shuttle," AIAA Paper 84-0225, Jan. 1984.

[14]Swaminathan, S., Kim, M. D., and Lewis, C. H., "Nonequilibrium Viscous Shock-Layer Flows over Blunt Sphere-Cones at Angle of Attack," *Journal of Spacecraft and Rockets,* Vol. 20, No. 4, 1983, pp. 331-338.

[15]Kim, M. D., Swaminathan, S., and Lewis, C. H., "Three-Dimensional Nonequilibrium Viscous Shock-Layer Flow over the Space Shuttle Orbiter," *Journal of Spacecraft and Rockets,* Vol. 21, No. 1, 1984, pp. 29–35.

[16]Song, D. J., and Lewis, C. H., "Hypersonic Finite-Rate Chemically Reacting Viscous Flows Over an Ablating Carbon Surface," *Journal of Spacecraft and Rockets,* Vol. 23, No. 1, 1986, pp. 47–54.

[17]Bhutta, B. A., and Lewis, C. H., "Low Reynolds Number Flows Past Complex Multiconic Geometries," AIAA Paper 85-0362, Jan. 1985.

[18]Bhutta, B. A. and Lewis, C. H., "An Implicit Parabolized Navier-Stokes Scheme for High-Altitude Reentry Flows," AIAA Paper 85-0036, Jan. 1985.

[19]Bhutta, B. A., and Lewis, C. H., "Prediction of Three-Dimensional Hypersonic Reentry Flows Using a PNS Scheme," *Journal of Spacecraft and Rockets,* Vol. 26, No. 1, 1989, pp. 4–13.

[20]Bhutta, B. A., and Lewis, C. H., "PNS Prediction of Three-Dimensional Hypersonic Flows with Strong Cross-Flow Effects," AIAA Paper 88-2696, June 1988.

[21]Bhutta, B. A., and Lewis, C. H., "Large-Angle-of-Attack Viscous Hypersonic Flows Over Complex Lifting Configurations," AIAA Paper 89-0269, Jan. 1989.

[22]Bhutta, B. A. and Lewis, C. H., "Three-Dimensional Hypersonic Nonequilibrium Flows at Large Angles of Attacks," *Journal of Spacecraft and Rockets,* Vol. 26, No. 3, 1989, pp. 158–166.

[23]Bhutta, B. A., Song, D. J, and Lewis, C. H., "Nonequilibrium Viscous Hypersonic Flows Over Ablating Teflon Surfaces," AIAA Paper 89-0314, Jan. 1989.

[24]Bhutta, B. A., Lewis, C. H., and Kautz, F. A., II, "A Fast Fully-Iterative Parabolized Navier-Stokes Scheme for Chemically-Reacting Reentry Flows," AIAA Paper 85-0926, June 1985.

[25]Peyert, R., and Viviand, H., "Computations of Viscous Compressible Flows Based on the Navier-Stokes Equations," AGARD-AG-212, 1975.

[26]Kaul, U. K., and Chaussee, D. S., "A Comparative Study of the Parabolized Navier-Stokes (PNS) Code Using Various Grid Generation Techniques," AIAA Paper 84-0459, Jan. 1984.

[27]Schiff, L. B., and Steger, J. L., "Numerical Simulation of Steady Supersonic Viscous Flows," AIAA Paper 79-0130, Jan. 1979.

[28]Shanks, S. P., Srinivasan, G. R., and Nicolet, W. E., "AFWAL Parabolized Navier-Stokes Code: Formulation and User's-Manual,"

Air Force Flight Dynamics Lab., Wright-Patterson AFB, OH, AFWAL-TR-823034, June 1979.

[29]White, F. M., *Viscous Fluid Flow,* McGraw-Hill, New York, 1974, pp. 28–30.

[30]Miner, E. W., Anderson, E. C., and Lewis, C. H., "A Computer Program for Two-Dimensional and Axisymmetric Nonreacting Perfect Gas and Equilibrium Chemically Reacting Laminar Transitional and/or Turbulent Boundary Layer Flows," Virginia Polytechnic Institute, Blacksburg, VA, VPI-E-71-8, May 1971.

[31]Peng, T. C., and Pindroh, A. L., "An Improved Calculation of Gas Properties at High Temperatures," The Boeing Company, Seattle, WA, Air D2-11722, 1962.

[32]Neumann, R. D., and Patterson, J. L., "Results of an Industry Representative Study of Code to Code Validation of Axisymmetric Configurations at Hypervelocity Flight Conditions," AIAA Paper 88-2691, June 1988.

[33]Patterson, J. L., private communication, Dec. 1988.

[34]Bhutta, B. A., Song, D. J., and Lewis, C. H., "Nonequilibrium Viscous Hypersonic Flows Over Ablating Teflon Surfaces," AIAA Paper 89-0314, Jan. 1989.

Walter B. Sturek
Associate Editor